pdFOAM: A PIC-DSMC Code for Near-Earth Plasma-Body Interactions

C. J. Capon[a,*], M. Brown[a], C. White[b], T. Scanlon[c], R. R. Boyce[a]

[a]*School of Engineering & Information Technology, University of New South Wales Australia, 2610, Australia*
[b]*Department of Mechanical and Aerospace Engineering, University of Strathclyde, Glasgow G1 1XJ, UK*
[c]*School of Engineering, University of Glasgow, GlasgowG12 8QQ, UK*

Abstract

Understanding the interaction of the near-Earth space environment with orbiting bodies is critical, both from a design and scientific perspective. In Low Earth Orbit (LEO), the interaction between the ionosphere and orbiting objects is well studied from a charging perspective. Not well understood is the effect of the ionosphere on the motion of LEO objects i.e. charged aerodynamics. This paper presents the implementation, validation, and verification of the hybrid electrostatic Particle-in-Cell (PIC) - Direct Simulation Monte Carlo (DSMC) code, pdFOAM, to study both the neutral and charged particle aerodynamics of LEO objects. The 2D aerodynamic interaction of a cylinder with a fixed uniform surface potential of -50 V and mesothermal O^+ and H^+ plasmas representative of ionospheric conditions is investigated. New insights into the role of bounded ion jets and their effect on surface forces are presented. O^+ bounded ion jets are observed to cause a 4.4% increase ion direct Charged Particle Drag (dCPD), while H^+ ion jets produce a net reduction in H^+ drag by 23.7% i.e. they cause a thrust force. As a result, we conclude that past work, primarily based on Orbital Motion Limited theory, does not adequately capture the physics of LEO charged aerodynamics. Hence, we recommend a revisit of conclusions regarding the significance of CPD to LEO objects - pdFOAM being an appropriate tool for this purpose.

Keywords: PIC-DSMC; Spacecraft interactions; Charging; Aerodynamics

1. Introduction

The interaction of near-Earth bodies, ranging from Low Earth Orbit (LEO) to Geosynchronous Earth Orbit (GEO), with the space environment leads to many technical and scientific challenges (see reviews [26, 29]). The LEO space environment ($100 - 2000km$ altitude) can be described as a cold, partially ionised, high-density plasma when compared to the fully ionised plasma found in GEO. The build-up of charge on a spacecraft surface has been shown to be a significant source of spacecraft anomalies (defined as an unplanned service outage, mission degradation or failure, data loss, sensor degradations, etc.). Koons et al. [36] reviewed 326 spacecraft anomalies related to environment interactions, 162 of which were related to electrostatic discharges (ESD) and charging; the remainder caused single event upsets (85), radiation damage (16) and miscellaneous phenomena (36). A recent study of the unexplained along-track decelerations of the LAGEOS-I and LAGEOS-II spacecraft - spherical satellites with nominal altitudes of 5900 km - by Andres [4] highlighted potential importance of Charged Particle Drag (CPD) to the motion of near-Earth objects - a field that has largely languished since the 1960s.

The 1963 review of charged particle aerodynamics by Brundin [14] concluded that effect on the motion of LEO objects from both the drag resulting from direct ion-surface collisions (dCPD) and indirect momentum exchange through dynamics friction type mechanisms (iCPD) due to O^+ dominated plasmas was negligible compared Neutral Particle Drag (NPD). Brundin [14]'s conclusions were based on the assertion that LEO spacecraft surface potentials never became more negative than -0.75 V, a statement supported by major works of the era

*Corresponding author
Email address: c.capon@student.unsw.edu.au (C. J. Capon)

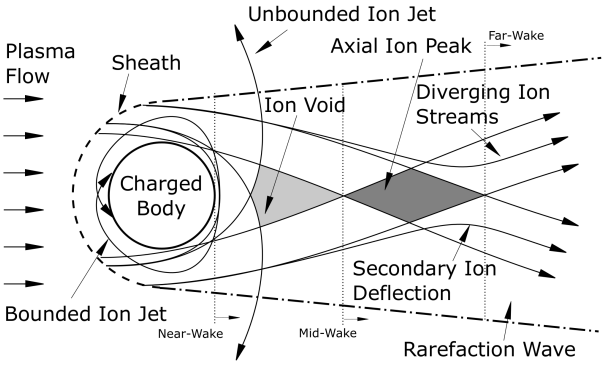

Figure 1: Schematic of LEO plasma-body interaction features.

[25, 56, 57]. The growing sophistication of spacecraft, particularly in LEO, has lead to an increased interest in the interaction of highly charged space platforms with the LEO environment [26, 29] (see [53, 54] for example).

Recent reviews of spacecraft charging in LEO [26, 29] recognise spacecraft surface potentials may achieve significant voltages relative to the surrounding environment both naturally and artificially. Anderson [3] presented a statistical study of 1600 charging events (defined as spacecraft charges exceeding -100 V) on the DMSP spacecraft at 840 km during auroral crossings. Meanwhile, the International Space Station (ISS) surface potential is artificially maintained at -30 V but would otherwise float around -110 V to -160 V as a result of the power requirements [29]. A recent study of the LAGEOS-I and LAGEOS-II spacecraft, with a nominal altitude of 5900 km, provides *in-situ* evidence that CPD can have a significant effect on the motion of orbiting objects.

Though above LEO, Andres [4] concluded that the contribution of CPD to the LAGEOS-I and LAGEOS-II spacecraft along-track accelerations increases from -0.5 pms^{-2} when not in eclipse to -85 pms^{-2} and -70 pms^{-2} respectively in eclipse - the larger eclipse CPD for the LAGEOS-I a reflection of its orbit which brings it over the auroral and polar zones and, hence floating potentials. Andres [4]'s CPD analysis was based on work by Hutchinson [32], itself based on Orbital Motion Limit (OML) theory [1], and was developed to predict the forces on a dust particle immersed in a flowing plasma - a physically similar interaction to that experienced by the LAGEOS spacecraft. OML makes critical assumptions regarding structure of plasma-body interactions. OML assumes that the plasma sheath, the region of charge discontinuity surrounding a charged body in a plasma, is spherically/cylindrically symmetric, much larger than body dimensions and the absorption barriers are not present. These assumptions are not appropriate for all LEO plasma-body interactions.

LEO plasma-body interactions are equivalent to the interaction between a negatively charged body and mesothermal flowing plasma, where ions and electron drift velocity are hyperthermal and subthermal respectively compared to the body. The resulting structure of these interactions is characterised by a compressed fore-body plasma sheath, elongated wake sheath surrounding on an ion rarefaction wave [50]. Figure 1 illustrates the main features of LEO plasma-body interactions. The anisotropic structure of the plasma sheath (discussed in Section 5) breaks down fundamental OML assumptions applied by past theoretical investigations of CPD [2, 14–16, 24, 34, 51]. To accurately determine the contribution of CPD to LEO objects requires a self-consistent approach that accounts for both the coupling of ions and body charge distributions, and, where suitable coupling, between neutral and charged particles. The increase in computational power and advances in numerical methods means that it is now possible to simulate the self-consistent interaction between neutral particles, charge particles and LEO objects.

Kinetic methods, such as the Direct Simulation Monte Carlo (DSMC), Particle-in-Cell (PIC) and Test Particle Monte Carlo (TPMC), indirectly provide solutions to the Boltzmann equation by simulating the microscopic interactions between a large number of macro-particles [7, 10], each macro-particle representing a large number of real particles. Kinetic methods can be further grouped by the Coulomb collision parameter [20],

$$\Lambda = 4\pi n_i \lambda_{D,e}^3 \tag{1}$$

where n_i is the ion number density and $\lambda_{D,e}$ is the electron Debye length (mean distance required to electrically screen two point charges in a plasma).

Figure 2 illustrates the applicability of a selection of computational methods to different classes of problem defined by Λ through altitude with approximate mean free path λ (based on the Hard Sphere (HS) model) and $\lambda_{D,e}$. Physically, systems dominated by binary particle collision phenomena are those with $\Lambda << 1$ i.e. electrical disturbances

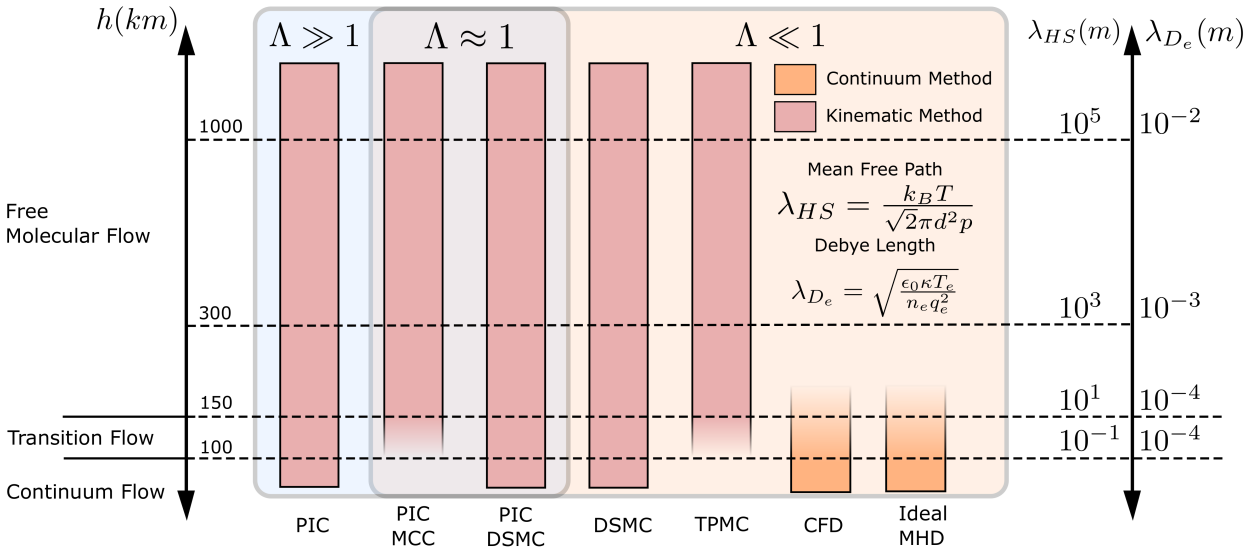

Figure 2: Applicability of computational methods to the simulation of the near-Earth environment.

are strongly damped by particle-particle collisions [20]. Comparatively, systems governed by collective phenomena are those with $\Lambda >> 1$ [20]. Not captured in Figure 2 is the effects of out-gassing or ion thrusters which can cause localised increases in both neutral and ion density about the body and must account for ion-neural coupling. The exploration of CPD, NPD in LEO, including the effects of neutral-ion coupling near active structures or below 300 km, requires a PIC-DSMC approach.

A majority of PIC codes developed for space-based applications (PicUp3D [22], CPIC [18], DEMOCRITUS [37], and DiP2/3D [42]) have been developed to study the charging of satellites and instrument calibration. As a result, they do not include gas-surface interaction models found in DSMC codes. Similarly, PIC-DSMC codes developed for space applications are primarily focused toward the investigation and design of plasma thrusters e.g. PICLas [5], DRACO [13]. To date, none of these codes has investigated the self-consistent interaction of the ensemble near-Earth space environment (both neutral and charged species) on the aerodynamics of orbiting objects or the influence that coupling between neutral and charged species has on NPD and CPD.

The purpose of this paper is to describe the implementation, validation and verification of pdFOAM; an electrostatic PIC-DSMC code developed in OpenFOAM [33] as an extension of the DSMC code, dsmcFOAM [47, 48], for investigating the influence of both NPD and CPD on near-Earth objects. Section 2 is primarily instructive, providing background theory to the PIC and DSMC methods. Section 3 outlines the implementation of pdFOAM and demonstrates the ability of pdFOAM to reproduce fundamental phenomena. Section 4 verifies the DSMC and PIC portions of pdFOAM with code-to-code comparisons with MONACO and PICLas respectively. Section 6 concludes with a practical example, presenting new insights into the role of bounded ion jets to dCPD on a LEO cylinder at a fixed floating potential of -50 V in O^+ and H^+ plasmas. The effect of iCPD (described in detail in [14]) is not considered in this work.

2. Kinetic Methods: Background and Theory

This section provides a brief description of the kinetic theory and its relationship to the PIC and DSMC methods. For an in-depth discussion of the PIC and DSMC methods, we refer to reader to [10] and [7] respectively. Similarly, [20] and [30] provide comprehensive descriptions of numerical methods specific to particle modelling techniques. The MKS system of units is used throughout this work unless stated otherwise.

2.1. Governing Equations

The near-Earth space environment can be regarded as a collection of positive ions, negative

electrons, and neutral atoms and molecules. Let us defined the phase space distribution function f of particles of species k within the volume element $dx_1 dx_2 dx_3$ as $f_k(\mathbf{x}, \mathbf{c}_k, t)$, where $\mathbf{c}_k$ and $\mathbf{x}$ are the particle velocity and position respectively at time t. Given a particular f_k, macroscopic mean properties arise from the moments of f_k e.g. number density (n_k) and velocity (v_k) [21],

$$n_k = \int f_k d\mathbf{c}, \qquad \mathbf{v}_k = \frac{1}{n_k} \int \mathbf{c}_k f_k d\mathbf{c} \tag{2}$$

At its most general, the evolution of f_k through t is described by the Boltzmann equation [12],

$$\frac{\partial f_k}{\partial t} + \mathbf{c}_k \cdot \nabla_x f_k + \frac{\mathbf{F}_k}{m_k} \cdot \nabla_c f_k = \left(\frac{\partial f_k}{\partial t} \right)_{coll} \tag{3}$$

From left to right, the terms on the LHS of Eqn. 3 describe: the rate of change of f_k with time; the diffusion of f_k; and the influence of external forces $\mathbf{F}_k$ acting on f_k. The RHS of Eqn. 3 describes the rate of change of f_k as a result of particle collisions. In a plasma, Eqn. 3 describes the interaction of particles of mass m_k and charge q_k through their mutual electric $\mathbf{E}$ and magnetic $\mathbf{B}$ fields via the Lorentz force ($\mathbf{F_k}$) [12, 20],

$$\mathbf{F}_k = q_k \left(\mathbf{E}(\mathbf{x}, t) + \mathbf{c}_k \times \mathbf{B}_k(\mathbf{x}, t) \right) \tag{4}$$

In the context of near-Earth plasma-body interactions, the interaction may be considered electrostatic and unmagnetized [37, 50, 55, 56]. Under these assumptions, Maxwell's equations reduce to Poisson's equation for the electric potential ϕ,

$$\mathbf{E} = -\nabla\phi, \qquad \nabla^2\phi = -\frac{\rho_c}{\epsilon_0} \tag{5}$$

where ϵ_0 is the permittivity of free space and ρ_c is the total macroscopic space-charge density from K ion species,

$$\rho_c \quad = \sum_k^K q_k \int f_k d\mathbf{c}_k = \sum_k^K q_k n_k \tag{6}$$

Determining the general particle distribution of a system with multiple reacting species in the presence of external and self-consistent forces is the challenge posed by kinetic theory. Direct solutions of the Boltzmann equation become intractable for practical systems [6]. Kinetic methods, such as the PIC [10] and DSMC [7] methods, avoid solving the Boltzmann equation directly by simulating the microscopic interactions of macro-particles.

2.2. The Direct Simulation Monte Carlo Method

The DSMC method describes collision dominated systems ($\Lambda << 1$) i.e. where the collision kernel $(\partial f_k/\partial t)_{coll}$ drives the evolution of f_k [7]. Applying the *"molecular chaos"* assumption - *"velocities of colliding particles are uncorrelated, and independent of position"* [40] -, the basis of the DSMC method is the *ad hoc* assumption that particle motion and collisions are decoupled over the small time-step Δt [7]. During a DSMC *"push"* step, simulated macro-particles are moved ballistically over Δt. During the collision step, Markov processes, implied by the molecular chaos assumption, describe the interaction of macro-particles according to kinetic theory [20, 52]. Phenomenological collision models approximate the physical interaction to varying degrees of fidelity (see Hard Sphere (HS), Variable Hard Sphere (VHS), and Variable Soft Sphere (VSS) described in [7]). Macroscopic properties are then sampled directly from the particle distribution, as in Eqn. 2, by applying time-averaging or ensemble-averaging for steady-state or transient systems respectively.

A common feature in most DSMC collision procedures involves the sorting of macro-particles into *"collision cells"* [9, 48], the exception being gridless DSMC methods [43, 44]. In collision cell approaches, candidate collision pairs are selected from a computational cell based on collision rates described by kinetic theory [7]. Collision pairs then undergo an acceptance-rejection test e.g. the No-Time-Counter (NTC) method [7]. The basis of the NTC method lays in determining the differential scattering cross-section (σ) between particle p and q i.e. σ_{pq}. Calculation of σ_{pq} is through a phenomenological model, where semi-empirical coefficients are tuned to match collision rates and viscosity coefficients at a reference temperature ($(T_{ref})_{pq}$). A list of VHS and VSS coefficients may be found in [9].

2.3. The Particle-in-Cell Method

The PIC method determines solutions to the Vlasov-Maxwell system where the contribution of collisions in Eqn. 3 are neglected i.e. collective dominated systems ($\Lambda >> 1$). The numerical realization of the PIC method is similar to the DSMC method. Macro-particle trajectories are traced through time using appropriate integration techniques e.g. the Leapfrog or Boris methods [30]. ρ_c is calculated by weighting the contribution of

macro-particles p to a computational mesh with nodes n according to some shaping function S [10] and *vice versa*, i.e.,

$$\rho_{c_n} = \sum_p q_p S(\mathbf{x}_n - \mathbf{x}_p) \tag{7}$$

The processes of determining ρ_c and $\mathbf{E}$ at a macro-particle are referred to as the *"assignment"* and *"interpolation"* steps respectively. Figure 3 illustrates the concept of charge assignment in one dimension; higher order shaping functions reducing numerical fluctuations in ρ_c as particles traverse cells [10].

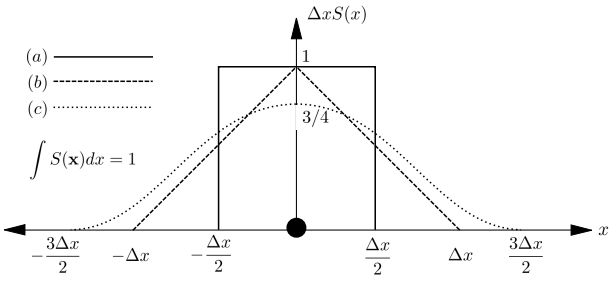

Figure 3: Shaping functions for charge and fields: (a) nearest grid point; (b) linear; (c) second-order.

Birdsall and Langdon [10] provide a comprehensive review of the numerical issues inherent in the coupling of particle and field domains through S. Key points are: the shaping functions must conserve charge between assignment and interpolation steps; the same shaping function must be applied between the assignment and interpolation steps to avoid numerical self-forcing (self-forcing being a purely numerical force on a particle caused by its own charge).

3. pdFOAM: Implementation

The electrostatic PIC-DSMC code, pdFOAM, has been developed to investigate the ensemble aerodynamics of near-Earth objects. pdFOAM has been developed in Open-Source C++ CFD library, OpenFOAM [33], as an extension of the DSMC code, dsmcFOAM (see [48] for implementation and validation of dsmcFOAM). Figure 4 illustrates a standard computational cycle in pdFOAM. The following sections outline Figure 4 in more detail and describe the implementation and validation of novel modules implemented in pdFOAM.

3.1. Overview of pdFOAM

pdFOAM supports both fully-kinetic (FK) and hybrid-fluid kinetic (HK) simulations. FK simulations model neutral, ion, and electron particle distributions directly; HK simulations approximate the electron particle distribution by a non-linear Boltzmann electron fluid (EF) (see Section 3.3). Both HK and FK pdFOAM simulations begin by solving for $\mathbf{E}$ given an initial particle distribution and use this field to set up the Leapfrog method, a time-centered particle integration technique [10]. At this point, the computational cycle outlined in Figure 4 begins:

1. Particles are pushed to a new position and boundary models are applied. The particle tracking algorithm is described in [39].
2. Cell occupancy is updated to include boundary interactions e.g. particle injection, deletion, reaction.
3. Collision partners are selected. To reconcile disparate spatial discretization requirements of the PIC and DSMC methods pdFOAM implements a new collision selection procedure; the Transient Conglomerated Cell (TCC) method (see Section 3.4).
4. Collision pairs are collided. pdFOAM supports HS, VHS and VSS phenomenological collision models, including reactions, with the Larsen-Borgnakke and Quantum-Kinetic (Q-K) energy redistribution models [47].
5. Particle cell occupancy is updated to account for the creation/annihilation of reacting particles.
6. Charge is weighted to the mesh domain to determine ρ_c. pdFOAM supports nearest volume (NV) and Composite Linear Volume (CLV) shaping functions (see Section 3.2).
7. Poisson's equation is solved using a preconditioned conjugate gradient Finite Volume Method (FVM) supplied in OpenFOAM [33]. Newton's method is used in HK simulations to solve the non-linear contribution of the Boltzmann electron fluid.
8. Fields are weighted to particles using the inverse shaping function of step 6.

The above process is repeated until the system either; achieves a steady-state, is identified as transient, or the simulation reaches a predefined end condition. In this work, we define steady-state

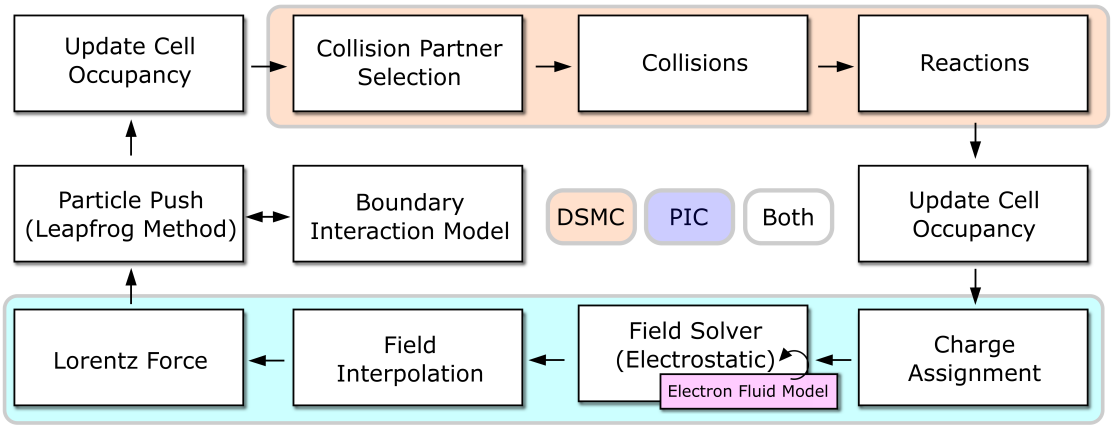

Figure 4: Standard computational cycle in pdFOAM with DSMC, PIC and PIC-DSMC methods colored

as when the total number of particles, charge in the system, and linear kinetic and potential energy of the system achieves a dynamic equilibrium. HK simulations are used to quickly reach a steady-state whereupon, FK simulations may be initialised based the HK solution to reduce total computation time. This is equivalent an initial value problem, the electron fluid number density distribution used to initialise particles based on the local number density compared to an initial homogeneous distribution. The effect of electron kinetics, including instabilities, on the HK solution can then be investigated as perturbations to the steady-state solution.

3.2. Composite Linear Volume Method

The CLV method applies multiple linear weighting functions to transform from particle to cell nodes and then cell nodes to cell volumes in logical space (l). The physical to logical space transformation uses the tri-linear interpolation method described in [46]. The concept of performing particle assignment and interpolation in PIC codes has been successfully demonstrated by the CPIC [18] and DEMOCRITUS [37] codes.

The charge assignment step determines the inverse linear volume weighting centered at the particle position to cell verticies. The charge is then distributed to surrounding cell verticies and weighted to the surrounding volumes. After solving for the field distribution, fields are interpolated back to particle positions using the inverse the the charge assignment process. Given the cell occupied by the particle, the surrounding cell nodes gather volume weighted fractions of surrounding field quantities and then interpolate these back onto the particle using a linear volume gather (summation instead of decomposition). Figure 5 illustrates the charge assignment and field interpolation processes with the linear weighting function shown in Eqn. 8.

$$
\begin{aligned}
\rho_{c_n}(i,j) &= \frac{q_i}{A_c}\frac{(\Delta x - x)(\Delta y - y)}{\Delta x \Delta y} \\
\rho_{c_n}(i+1,j) &= \frac{q_i}{A_c}\frac{x(\Delta y - y)}{\Delta x \Delta y} \\
\rho_{c_n}(i,j+1) &= \frac{q_i}{A_c}\frac{(\Delta x - x)y}{\Delta x \Delta y}, \\
\rho_{c_n}(i+1,j+1) &= \frac{q_i}{A_c}\frac{xy}{\Delta x \Delta y}
\end{aligned}
$$

The advantage of the CLV method is that it allows the use of cell-centered numerical methods without needing to employ co-located or staggered meshes, while also facilitating parellisation (shared nodes passing data across processors). OpenFOAM uses FVMs and does not currently support co-located or staggered grids. The CLV method fills the niche for cell-centered data on a single grid at the expense of increased computation expense compared to the co-located grid approach. As an alternative, pdFOAM also includes a NV approach were charge is assumed to be uniformly distributed within the cell occupied by the particle - equivalent to a Nearest-Grid-Point (NGP) approach. At the expense of physical fidelity, the NV offers a significantly faster alternative to the CLV method in pdFOAM.

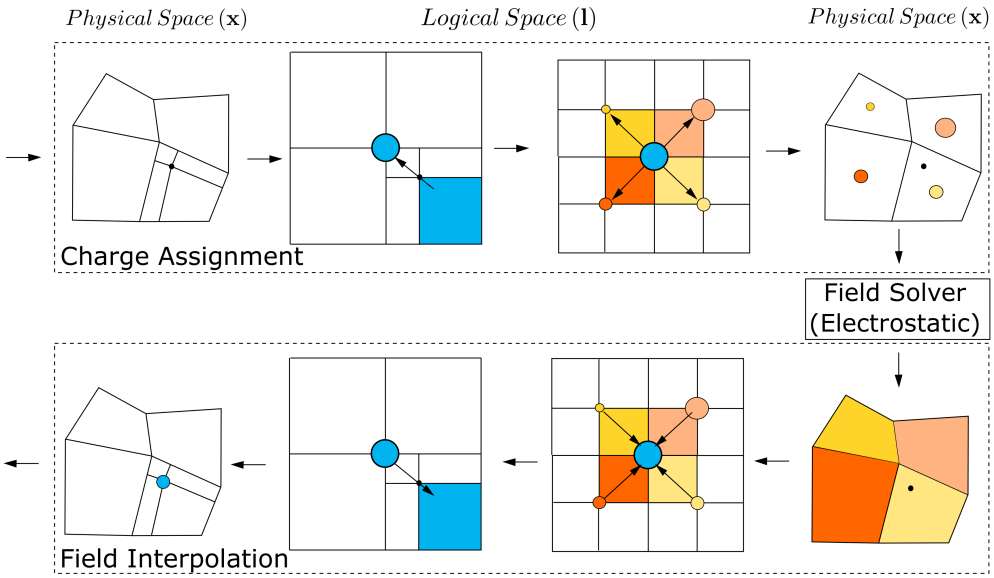

Figure 5: Illustration of CLV method applied in Charge Assignment and Field Interpolation steps. Only the process for a single node/particle is shown for brevity.

3.2.1. CLV Validation: Electron Oscillations

Ascribing finite-sizes through S to macro-particles may result in several numerical artifacts in PIC methods e.g. the addition of numerical energy. The idealised 1D oscillation of an electron about a stationary ion due to a small separation (Δx_{sep}) is a simple and instructive test shaping functions. The electron motion can be expressed as a simple harmonic oscillator described by,

$$\begin{aligned} X(t) &= \Delta X_{sep} \cos(\omega_{pe} t) \\ U_x(t) &= -\Delta X_{sep} \omega_{pe} \sin(\omega_{pe} t) \end{aligned} \tag{8}$$

where ω_{pe} is the plasma oscillation frequency.

To test implementation of the NV and CLV method in pdFOAM, the oscillations of an electron about a fixed ion were investigated. A $1mm$ domain was sub-divided into 200 cells in x, an ion at 0.5025 mm (cell center) and a stationary electron at 0.5125. Figure 6 plots the electron osculations through time with $\Delta t = 1 \times 10^{-9} s$ over a period of $1 \times 10^{-5} s$ (10000 steps) in position-velocity phase-space calculated using the NV and CLV shaping functions respectively. Motion in X demonstrates that neither method adds a significant amount of numberical energy over the simulated period, the oscillation amplitude remaining constant. Motion in U_x illustrates the aliasing effect of the NV method, a_x constant throughout each cell and 0 in the central cell. Comparatively, the CLV method provides a significantly better approximation of the electron's motion, marginally underpredicting U_x compared to the NV method. Hence we conclude that both the NV and CLV methods don't add numerical energy, the CLV method providing a more physical approximation of plasma interactions. PIC simulations generally not interested in single particle motion, better suited to Molecular Dynamics (MD) methods, but in collective phenomena [10].

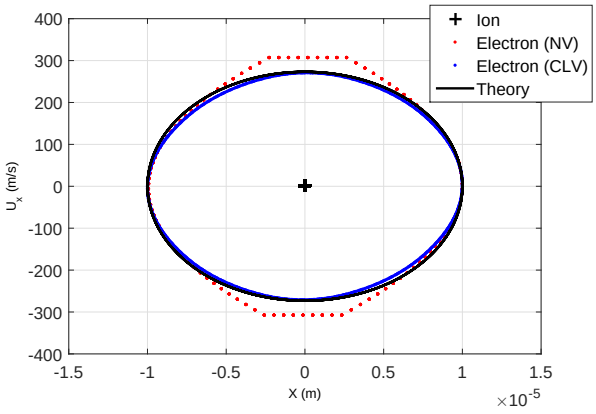

Figure 6: Theoretical 1D electron oscillation about stationary ion compared to observed oscillation in pdFOAM.

3.3. Non-Linear Boltzmann Electron Fluid Model

Directly simulating electrons comes at a significant computational cost. To maintain numerical stability, Δt must be smaller than the fastest plasma frequency ω_p, such that $\Delta t < \omega$ [20] [1][20]. In a similar manner, the stability requirements of the leapfrog method (see [30]) require a spatial discretization (Δx) of $\Delta x < \lambda_{D,e}/2$. By replacing the electron particle distribution with a fluid allows HK simulations to employ timesteps $10^2 - 10^6$ larger than equivalent FK simulations depending on specific system configurations. The benifits of a larger time step and reduction in simulated particles (no electrons) often outweighing the computational cost of solving, in this case, the non-linear Poisson's equation (see below). For these reasons, there are significant speedups if a fluid can approximate the electron distribution.

The approach taken here is to assume that the electron distribution function can be described by an isothermal, currentless (electrostatic), unmagnetized ($\mathbf{B} = 0$), inertia-less ($m_e/m_i \to 0$) electron fluid (EF); this approach has been used successfully for the study of plasma-body interaction from a charging/arcing context [54] and in the analysis of plasma thrusters [11]. Under these assumptions, magnetohydrodynamic equations of continuity, momentum, and energy reduce to [11],

$$n_e = n_{e,\infty} \exp\left[\frac{q_e(\phi(\mathbf{x}) - \phi_\infty)}{k_B T_e}\right] \tag{9}$$

where k_B is the Boltzmann constant, T_e the electron temperature, and $n_{e,\infty}$ the freestream electron number density and phi_∞ is the freestream reference potential.

Assuming a quasi-neutral freestream plasma ($n_i = n_e$), $\phi_\infty = 0$. Substituting Eqn. 9 into Poisson's equation gives a non-linear function of potential,

$$\epsilon_0 \nabla^2 \phi - q_e n_{e,\infty} \exp\left[\frac{q_e \phi}{k_B T_e}\right] = -q_i n_i \tag{10}$$

Applying Newton's method, solutions to Eqn. 10 become an iterative process in t,

$$\begin{aligned}\left(\epsilon_0 \nabla^2 - \frac{\epsilon_0}{\lambda_{D_e}^2} \exp\left[\frac{q_e \phi^{(t)}}{k_B T_e}\right]\right) \phi^{(t+1)} = \\ - q_i n_i + \left(q_e n_\infty - \frac{1}{\lambda_{D_e}^2} \phi^{(t)}\right) \exp\left[\frac{q_e \phi^{(t)}}{k_B T_e}\right]\end{aligned} \tag{11}$$

[1] $\Delta t < 0.01\omega$ is often used in fully-kinetic PIC simulations to avoid numerical heating of the electron distribution [10].

Hockney and Eastwood [30] demonstrated that the convergence of Eqn. 11 is quadratic provided the initial guess is sufficiently near the solution; this is the case for time-stepping simulations, such as the PIC method, where the initial solution t at time-step n is taken as the converged solution at $n - 1$.

3.3.1. EF Validation: Planar Sheath Structure

The interaction of a plasma with an immersed object can be complex; ranging from surface absorption, deep penetration, and neutralization, to the emission of other charged particles through secondary electron emission or sputtering [27, 45, 56]. Before considering such phenomena, it is essential to demonstrate that the plasma-body interaction is modeled correctly; this applies to both FK and HK simulations. The shielding of a perfectly conducting wall in an unmagnetized, collisionless, flowing plasma, consisting of electrons and singly charged ions, is suitable for this purpose. The following discussion outlines the theory describing the general structure of a 1D plasma sheath for a fixed wall potential. For a detailed analysis, we refer the reader to [45].

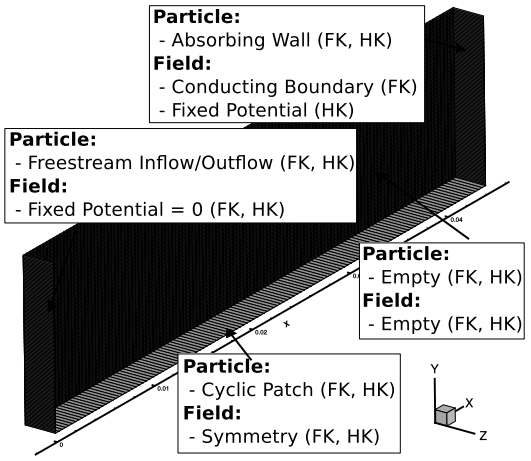

Figure 7: Computational setup of planar sheath case

Consider a freestream plasma at $x = 0$ such that it is sufficiently far from a large flat plate with a fixed potential ϕ_p at $x = L$ that the freestream may be considered quasi-neutral i.e. $\phi(0) = 0$ and $\phi(x) = \phi_p$. In the region between $x = 0$ and $x = L$ there must then exist some potential structure or *"plasma sheath"* shielding the freestream plasma

from the space-charge discontinuity at x. Given an ion drift velocity u_∞ and Boltzmann electrons, the dimensionless plasma sheath equation is described by [45],

$$\frac{1}{2}\psi'^2 = M^2\left[\left(1+\frac{2\psi}{M^2}^{1/2}-1\right)\right]+\exp\left[-\psi\right]-1 \tag{12}$$

Equation 12 can be expressed in closed form and solved numerically using the boundary condition $\psi(L)=\psi_p$, where the dimensionless position (ξ), potential (ψ) and ion acoustic Mach number (M_i) are defined as,

$$\begin{aligned}\xi &= \frac{x}{\lambda_{D_e}},\\ \psi(\xi) &= -q_e\phi(\xi)/k_BT_e,\\ M_i &= \frac{u_\infty}{(k_BT_e/m_i)^{1/2}}\end{aligned} \tag{13}$$

To demonstrate the ability of pdFOAM to reproduce sheath structure accurately, we compare the sheath structure defined by Eqn. 12 against pdFOAM for a H^+ plasma with $n_\infty = 1\times10^{12}m^{-3}$ and drift velocity 2.1 times it's thermal velocity at $1000K$ with a -0.1804 V wall. Maximum cell spacing was 1.7×10^{-5} m, while timestep was 1×10^{-9} s and 5×10^{-8} s for the FK and HK simulations respectively. Figure 7 illustrates the numerical setup with particle and field boundary conditions.

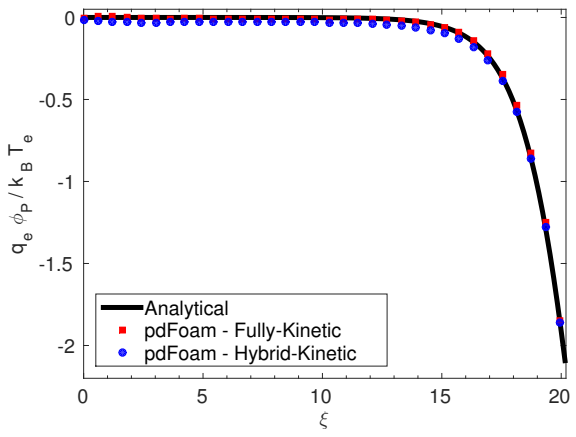

Figure 8: Comparison of numerical and analytical sheath structure (left) and computational setup (right)

Figure 8 compares the theoretical and numerical sheath potential structure. Motion is constrained in the Z axis while retaining three velocity components. Figure 8 shows that there is close agreement between FK, HK, and analytical ϕ distributions. The key difference being that the HK simulation does not exhibit an ion source sheath at the inlet as seen in the FK case. This is expected as the source sheath is a numerical product of re-fluxing electrons and the constant flux inlet boundary condition [49].

3.4. Transient Conglomerated Cell Method

The numerical requirements of DSMC and PIC methods differ. While both methods are stochastic as a result of their particle nature, the acceptance/rejection scheme in the DSMC collsion step applies a further stochastic method compared to the PIC method. DSMC best practice is to maintain a constant number of particles per cell throughout the flowfield to avoid numerically biasing a particular region [9]. Furthermore, the size of collision cells should not exceed $\lambda/3$ [9]. PIC cells must satisfy the requirement $\Delta x < \lambda_{D_e}/2$ in order for the leapfrog method to remain stable [30]. Hence, in general, PIC requirements limit PIC-DSMC simulations. As a result, PIC-DSMC simulations using a single mesh require orders of magnitude more particles than pure DSMC simulations to satisfy both the particles per cell and $\Delta x < \lambda_{D_e}/2$ requirements.

Several approaches have been proposed to reconcile the numerical requirements of the PIC and DSMC method [35, 44]. The Transient Conglomerated Cell (TCC) method implemented in pdFOAM is based on the approach taken in the DSMC codes DS2V/3V [9]. DS2/3V uses a fine background mesh to construct collision cells from a conglomeration of sub-cells about randomly scattered node points. Similarly, the TCC method constructs collision cells from the PIC mesh based on the instantaneous particle distribution at each time-step. Cell clusters are constructed by iterating out through cells with common face indices as illustrated in Figure 9 (a) - (c). Cell construction currently stops when the number of particles per collision cell exceeds a user defined number or the maximum cell dimension exceeds a user defined fraction of the local mean free path e.g. $\lambda(\mathbf{x})/3$.

The TCC method promotes nearest neighbor collisions by preferentially searching the collision cell decomposition to minimize mean collision distance. Figure 9 (d) and (e) illustrates the TCC collision partner selection procedure. First, a collision candidate p is selected randomly from the collision

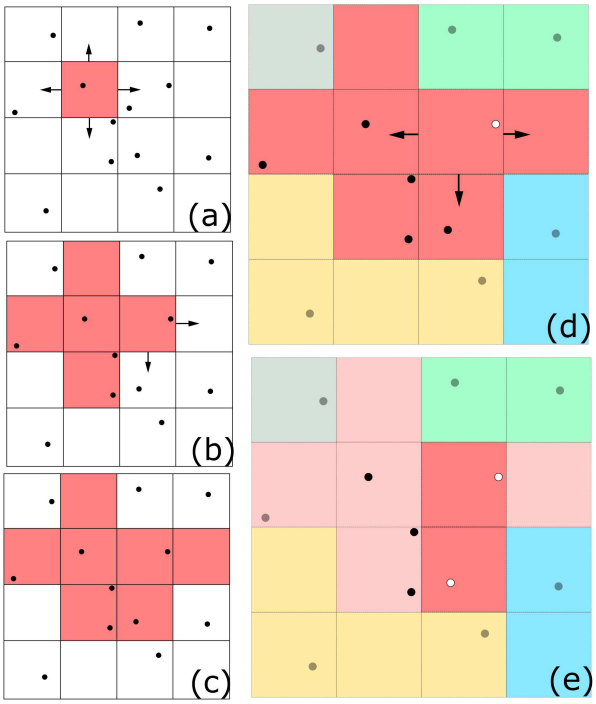

Figure 9: TCC collision cell procedure: (a) Collision cell construction begins, (b) Cells with common faces are added to collision cell, (c) Cells are iteratively added until construction requirements are met, (d) Cells surrounding candidate are searched (e) Closest cell containing collision candidates is selected and a partner randomly chosen.

cell. Next, adjacent collision sub-cells are iteratively searched to find the nearest cell containing particles. A collision candidate q is then randomly selected from this sub-cell.

As only an integer number of collisions may occur during a time-step, the remainder is isotropically distributed over the collision cell's sub-cells and carried forward to the next time-step. By linking the collision remainder to the mesh instead of collision cell index, the random motion of the collision cell index with respect to physical location does not cause the transport of collisions to non-physical locations.

3.4.1. TCC Validation: Adiabatic Heat Bath

DSMC simulations model the evolution of a system's particle distribution function f_k through an approximation of the Boltzmann collision kernel. It is, therefore, essential that a DSMC code accurately reproduces collision rates described by kinetic theory [6]. To ensure that the TCC method accurately captures collision rates consider a gas at thermal equilibrium with no gradients i.e. an adiabatic heat bath. The collision rates between species p and q is [6, 7],

$$(N_{pq})_0 = 2\pi^{1/2}(d_{ref})_{pq}^2 n_p n_q \left(\frac{T}{(T_{ref})_{pq}}\right)^{1-\omega_{pq}} \left(2k_B\frac{(T_{ref})_{pq}}{m_r}\right)^{1/2} \quad (14)$$

where d_{ref}, T_{ref} and ω are the VHS model parameters, reference diameter, reference temperature and viscosity component, respectively; n is the number density, k_B is the Boltzmann constant, T the overall temperature and m_r the reduced mass. The factor of 2 accounts for pq and qp collisions; for pp or qq collisions this must be removed.

To validate the TCC method, the collision rates of three different gas mixtures described by Eqn. 14 were compared against those computed by pdFOAM at various temperatures. Simulations used a $27x27x27$ mm cube with specular walls. The timestep was 1×10^{-7} s and cell spacing was 3×10^{-4} m. VHS collision properties are from [9]. Cases I and II simulate the collision rates for a single species O_2 and N_2 gas respectively. Case III simulates a $50\%O_2 - 50\%N_2$ gas mixture. Figure 10 shows that the TCC method accurately reproduces the increase in collision rate with temperature predicted by Eqn. 14.

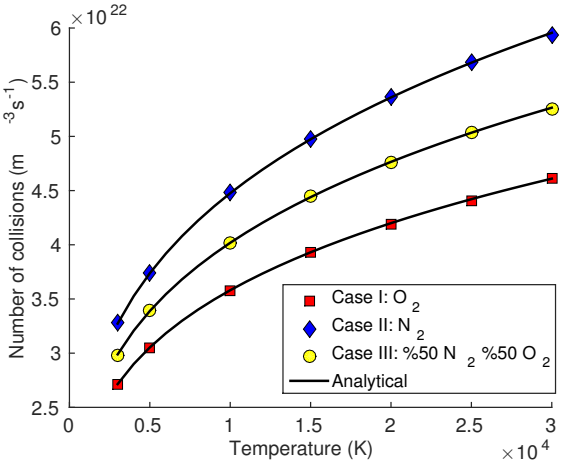

Figure 10: Comparison of numerical and theoretical collision rates using the TCC method.

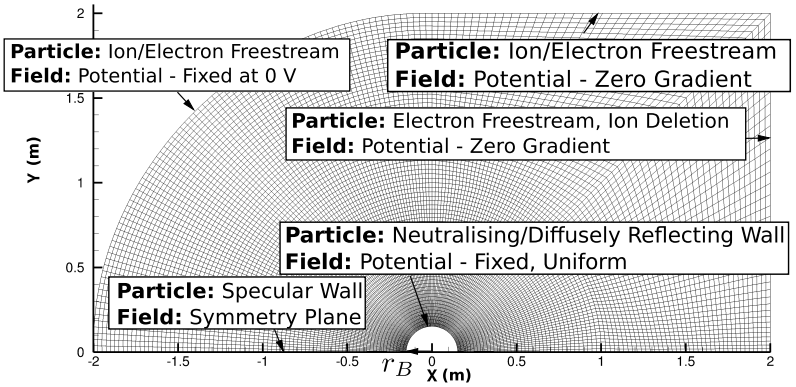

Figure 11: Domain topology and boundary conditions. Every 10th grid node displayed for clarity.

4. pdFOAM: Verification

Section 3 described the implementation of pdFOAM and presented fundamental validation cases. This section further develops confidence in the ability of pdFOAM to model the interaction of near-Earth objects with the space environment with two studies that verify the implementation of the PIC and DSMC methods in pdFOAM:

1. The Mach 10 $Kn = 0.2$ cylinder case from [38] is repeated and compared with data from MONACO [19], an established DSMC code.
2. The self-consistent charging of a flat plate and a cylinder in a flowing, collisionless, unmagnetized plasma is compared to theoretical predictions of floating potential at different ion drift velocities.

4.1. Simulation Topology

The following simulations are 2D and use a common cylinder topology with body radius r_B as illustrated in Figure 11. Figure 11 lists particle and field boundary conditions, while case specific boundary conditions are described in the appropriate sections. Mesh density is based on the mean plasma conditions experienced by the Earth Observation System (EOS) during a period of mean sunspot activity [28]; these conditions are listed in more detail in Section 4.3.

4.2. Hypersonic Cylinder

[38] investigated the breakdown of the continuum assumption on the aerothermodynamics of a hypersonic cylinder in a reacting flow. They investigated a Mach (M) 10 flow of Argon (Ar) over a two-dimensional, 12 in (0.3048 m) diameter cylinder with a fixed surface temperature of 500 K for a variety of Kn by varying the freestream number density (n_∞). The following sections outline the numerical setup of pdFOAM and compare with results in [38].

4.2.1. Numerical Setup

Freestream number density, temperature and velocity are $1.699 \times 10^{19} m^{-3}$, $200K$ and $2634.1 m/s$ respectively. Gas-surface interactions are that of a diffusely reflecting wall with complete thermal accommodation to a fixed surface temperature of $500K$. VHS coefficients are $T_{ref} = 1000K$, $d_{ref} = 3.959 \times 10^{-10} m$, and $\omega = 0.734$ to be consistent with [38].

4.2.2. Results and Discussion

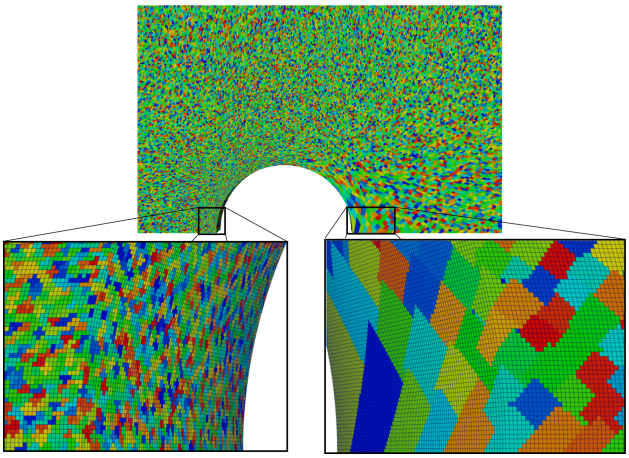

Figure 12: Visualisation of collision cells. Collision cell colours are random.

The total linear kinetic energy and number of simulated macro-particles achieved a dynamic equilibrium (steady-state) after 10,000 time-steps, with 1.6 million macro-particles in the system. At steady-state there were $\approx$ 1500 collision cells and a 99.9% reduction in collision cells loops compared to the full mesh ($\approx$ 4 million cells). Results were sampled over 60,000 time-steps after the steady-state had been reached to reduce statistical fluctuations. Figure 12 visualizes the conglomerated collision cells constructed in the fore-body (bottom left) and rear (bottom right) of the cylinder on the full mesh. Clustering of collision cells in Figure 12 demonstrates the ability of the TCC method to capture high and low density regions as well as the transition region with no *a priori* knowledge of the flow.

Figure 13 compares contours of temperature between pdFOAM (top) and MONACO (bottom). Figure 14 compares the surface pressure (c_P) and heat flux (c_H) coefficients.

$$c_P = \frac{2\left(P - P_\infty\right)}{\rho_\infty u_\infty^2} \qquad c_H = \frac{2Q}{\rho_{m_\infty} u_\infty^3} \tag{15}$$

where P is pressure, Q heat flux and ρ_m is the mass density.

There is good agreement between pdFOAM and MONACO; differences being a small increase in peak translational temperature in the ram position in the pdFOAM simulation and an extension of the "warm" region in near wake. The increased noise in pdFOAM results compared to MONACO appears a consequence of the higher spatial resolution (smaller cells), numerical fluctations enhanced by a reduction in particles per cell - the collision cells not used as sampling cells. The source of the extension of the "warm" region in the wake is unclear, most likely due to difference in collision partner selection. Nevertheless, overall there exists excellent agreement between flowfields.

Comparing surface coefficient, pdFOAM over-predicts peak c_P by 2.27% and under-predicts peak-heat flux by 2.7% compared to MONACO. A comparison of MONACO with other established DSMC codes for [38]'s $Kn = 0.009$ case show a 2.7% under-prediction of peak heat flux is within the code-to-code uncertainty reported in [8].

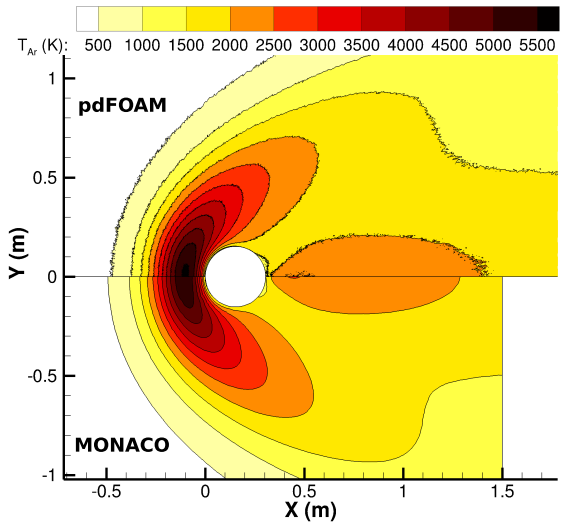

Figure 13: Contours of temperature: *pdFOAM* (top) and *MONACO* (bottom)

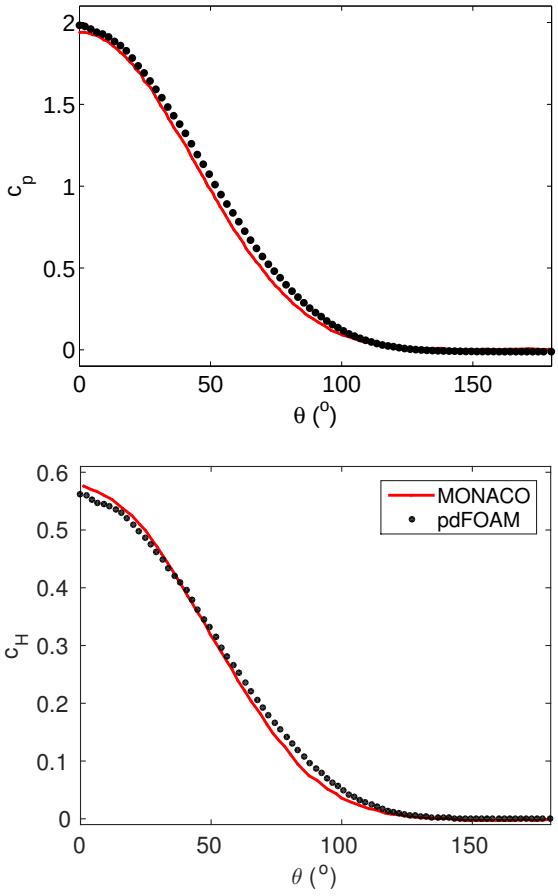

Figure 14: Comparison of *pdFOAM* and *MONACO* surface distributions: c_P (top) and c_H (bottom).

4.3. Self-Consistent Charging Simulations

The self-consistent charging of a body immersed in plasma is a complex problem in plasma physics [25, 26, 28]. Self-consistent charging requires accurate replication of both kinetic and boundary phenomena to reproduce the electron and ion current balance needed to achieve a dynamic equilibrium at floating potential ϕ_B.

pdFOAM supports both absorbing and catalytic walls, the former deleting incident particles, the latter transforming them into one or more particles. Reflected particles may be re-emitted in either a diffuse or specular manner with a degree of thermal accommodation to the wall. pdFOAM treats wall charging in one of three ways:

1. Perfectly Conducting Wall: Charge is distributed evenly across the surface before calculating fields. The effect of surface currents on the system is neglected
2. Perfectly Insulating Wall: Charge accumulates on wall cell faces and does not transport about the surface. Arcing is not currently considered.
3. Fixed Potential Wall: Charge is absorbed, and the surface potential remains fixed based on initial conditions.

The implementation of more advanced wall boundary conditions is the subject of ongoing work, the above being sufficient for the scope of the work presented here. The following sections outline relevant charging theory and numerical setup. Numerical and theoretical floating potentials are compared for a range of ion drift velocities.

4.3.1. Charging Theory

Consider the charging of a large, perfectly conducting, flat plate in a collisionless, unmagnetised, single ion species plasma, with ion drift velocity u_∞. In general, the electron thermal velocity $u_{t,e}$ is much larger than u_∞ and the electron distribution can be described by the Boltzmann factor [57]. As a result, the electron current (I_e) from random particle flux per unit surface area to a surface with potential ϕ_B is [57],

$$I_e = q_e n_{e_\infty} \left(\frac{8T_e k_B}{\pi m_e}\right)^{1/2} \exp\left(-\frac{q_e \phi(\phi_B)}{k_B T_e}\right) \quad (16)$$

As ion thermal velocity $u_{t,i} \to u_\infty$, the ion velocity distribution is described by a shifted-Maxwellian function [6],

$$f_i(v) = \left(\frac{m}{2\pi k_B T_i}\right)^{1/2} \exp\left[-\frac{m\left(v-u_\infty\right)^2}{2k_B T_i}\right] \quad (17)$$

where ion current (I_i) is given by,

$$I_i = q_e n_{i_\infty} \int_0^\infty v f_i(v) d^3 v \quad (18)$$

For a flat plate, Eqn. 18 becomes [57],

$$\begin{aligned} I_i &= q_e n_{i_\infty} u_\infty \frac{1}{2}\left(1 + \mathrm{erf}(y) + \frac{1}{\sqrt{\pi} S_i} \exp\left(-S_i^2\right)\right), \\ S_i &= u_\infty \left(\frac{2k_B T_i}{m_i}\right)^{-1/2} \end{aligned} \quad (19)$$

where S_i is the ion drift ratio.

The system reaches an electrical dynamic equilibrium when $I_i = I_e$. Equating Eqn. 16 and Eqn. 19, the floating potential of a large flat plate in a drifting plasma is described by,

$$\begin{aligned} \phi_p &= \frac{k_B T_e}{q_e}\left(ln\left(f\right) - ln\left(\sqrt{\frac{m_i}{2\pi m_e}}\right)\right), \\ f &= \frac{S_i}{\sqrt{2}}\left(1 + \mathrm{erf}(S_i) + \frac{1}{\sqrt{\pi} S_i} exp\left(-S_i^2\right)\right) \end{aligned} \quad (20)$$

The charging of a cylinder in a collisionless, unmagnetised, single species plasma, with drift velocity u_∞, is similar to the flat plate case but must also take into account conservation of angular momentum of ions about the body. In the Orbit Motion Limited (OML) regime, I_i can be approximated as, [31],

$$\begin{aligned} I_i &= I_{i,t} \frac{2}{\pi^{1/2}} \left(|\psi| + S_i^2 + \frac{1}{2}\frac{|\psi| + 1/2 S_i^2}{|\psi| + S_i^2}\right)^{1/2}, \\ &|\psi| + S_i^2 > 0, \psi = \frac{q_e \phi_B}{k_B T_e} \end{aligned} \quad (21)$$

where $I_{i(e),t}$ is the random ion(electron) thermal current to the surface with area A,

$$I_{i(e),t} = A q_e n_{i(e)} \sqrt{\frac{k_B T_{i(e)}}{2\pi m_{i(e)}}} \quad (22)$$

The electron current, similar to Eqn. 16, is given by,

$$I_e = I_{i(e),t} exp\left(-\frac{q_e \phi(\phi_B)}{k_B T_e}\right) \quad (23)$$

Equating Eqn. 21 and Eqn. 23, the floating potential for a given condition may be solved numerically - we employ Newton's method in this work.

Table 1: Computational parameters for charging simualtions

Parameters	Flat Plate	Cylinder
Plasma		
$n_{i/e,\infty}$ (m^{-3}	1×10^{12}	4×10^{10}
T_i (K)	1000	1537
T_e (K)	1000	1997
Body		
r_B (m)	-	0.03
Gas		
Species	H^+	O^+
m (kg)	1.67×10^{-27}	26.55×10^{-27}
Numerical		
ρ_{part}	2	45
Δt (s)	2.5×10^{-9}	5×10^{-9}
Case	$u_{H^+,\infty}$ (m/s)	$u_{O^+,\infty}$ (m/s)
I	0	0
II	6038	2722
III	11501	5445
IV	-	7500
V	-	9076

4.3.2. Numerical Setup

Flow and numerical properties for the flat plate and cylinder charging cases are listed in Table 1. Cylinder flow conditions are taken from [28] and represent the average conditions experienced by the EOS during a period of mean sunspot activity. Flat plate conditions are based on similar work in [18].

Gas-surface interactions used in both flat plate and cylinder charging simulations are that of a perfectly conducting, absorbing, wall, where incident particles are neutralized and removed from the simulation; this is appropriate as the system is collisionless i.e. neutral and charged species are decoupled. All simulations are fully-kinetic. At steady-state, as defined previously, simulations are averaged over $10,000$ time-steps to reduce the statistical scatter of the data.

4.3.3. Results and Discussion

Figure 15 compares theoretical floating potentials for a flat plate and a cylinder with those predicted by pdFOAM. There is good agreement between theory and simulation floating potentials for all flat plate cases. Cylinder floating potential is well predicted for $S_i > 2$; ϕ_B at $S_i = 0$ under-predicted by 1.6%.

Delzanno et al. [18] performed a similar charging simulation on an axi-symmetric sphere, observing a 1.6% over-prediction in floating potential which

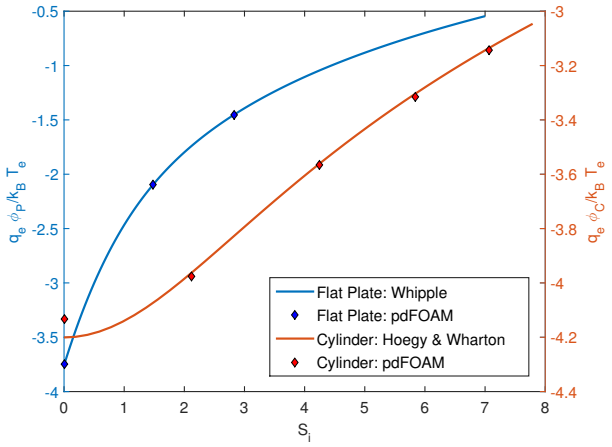

Figure 15: Comparison of theoretical and numerical surface potential for different flow speeds.

was attributed to the formation of ion absorption barriers [2, 17, 23]. The ion absorption barrier phenomena, discussed in detail in the following section, is not captured by OML approaches [2, 31]. Ion absorption barriers account for the under-prediction of ϕ_B as a result of an increased ion flux to the cylinder at $S_i = 0$. As the relative kinetic energy of the flow increases, the effect of absorption barriers becomes negligible and the floating potential approaches Eqn. 21 i.e. Eqn. 21 is valid for $\psi + S_i^2 > 0$ [31, 41]. pdFOAM accurately reproduces the self-consistent charging interaction of a perfectly conducting flat plate and a cylinder for a variety of drift velocities.

5. LEO Plasma-Body Interactions

Previous sections described the implementation, validation, and verification of pdFOAM. This section presents new insights into the role of ion absorption barriers, predicted by Orbital Motion (OM) theory, in the charged aerodynamic interaction of LEO objects with the ionosphere.

5.1. Ion Absorption Barriers

A collisionless plasma conserves both total energy and angular momentum. OM theory describes the radial motion of incident ions in a symmetric sheath using the effective potential energy U_{eff}[2, 23],

$$U_{eff}(r, L) = \frac{L^2}{r^2} + \frac{2q_i\phi(r)}{mv_\infty^2} \qquad (24)$$

where U_{eff} is normalised by the total freestream energy.

Here, the first term on the RHS is the normalized angular momentum about a point and the second term is the normalized potential energy. Ion motion is restricted to the region where $U_{eff} \leq 1$ i.e. if $U_{eff}(r, L) = 1$ has root(s), the largest determines the distance of closest approach r_c. Considering an attractive body ($\phi_B < 0$) the structure of $\phi(r)$ about a cylinder in a stationary plasma is a symmetric potential field. At large values of r, $d\phi(r)/dr < 1/r^2$, while near the body $d\phi(r)/dr < 1/r^2$ [23]. As a result, there may exist local inflections in Eqn. 24, determined by the condition [23],

$$r^3(d\phi/dr) = m_i v_\infty^2 \rho^2 \tag{25}$$

The maximum U_{eff} always occurs at a larger distance (r_M) than the minimum determined by the condition $dU_{eff}/dr(r_M) = 0$ and $dU_{eff}^2/d^2r(r_M) < 0$. If $U_{eff}(r_M) \geq 1$ for a particular $L(v)$) there exist multiple roots to $U_{eff}(r, L(v)) = 1$; physically these roots correspond to the presence of an absorption barrier that reflects ions about the body [2]. The transitional impact parameter L_* separates particle trajectories into those that do not experience a barrier potential ($L > L_*$) and those that do ($L \leq L_*$) [23],

$$L_* = r_M \left(1 - \frac{2q_i\phi(r_M)}{m_i v_\infty^2}\right)^{1/2} \tag{26}$$

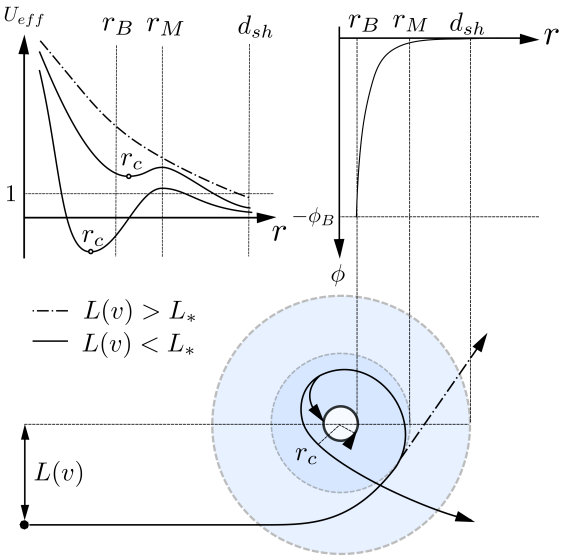

Figure 16: Illustration of ion orbital motion about a charged cylinder in a central force field.

Figure 16 illustrates the physical interpretation of the above analysis when an ion, with a particular $L(v)$, enters an attractive symmetric plasma sheath. As the ion travels through the sheath, it is deflected by the sheath. If $L(v) > L_*$, the ion goes through a small angle deflection ($\leq 90^0$). If $L(v) \leq L_*$, the ion passes through the local maximum in U_{eff} and enters an orbit about the body. When $r_c < r_B$, ions are collected by the body. LEO plasma-body interactions however, are characterized by a highly anisotropic sheath structure [50].

The anisotropic sheath structure is a result of a mesothermal ($v_{t,i} \ll v_B \ll v_{t,e}$) interaction. The resulting sheath structure is characterised by a compressed fore-body sheath and an extended wake sheath [2]. The deflection of ions to fill the wake region is enhanced by the fast moving electrons, which populate the near-wake ion void causing large localised negative potentials [50]. Behind this region, the confluence of the scattered ions can lead to a positive wake structure and, in turn, the secondary deflection of electrons [50]. The coupled nature of electron and ion distribution with sheath structure requires a self-consistent kinetic treatment of the problem. As we have discussed, one such method is the PIC method.

5.2. Ion Orbital Motion Structures in LEO

Figure 17 plots the ratio of potential to kinetic energy for the O^+ (bottom) and H^+ (top) flows at $\phi_B = -50$ V (condition are that of case IV in Table 1) with $r_B = 0.3$ m ($r_B/\lambda_{D,e} = 30$). Contours show the ratio of potential to kinetic energy, the governing parameter in Eqn. 26 large values corresponding to field dominated regions.

Here, the hyperthermal ion flow leads to a compressed fore-body plasma sheath and an ion void region in the wake; consistent with experiment [50] and numerical [41] observations. In response to the ion-void, an ion acoustic Mach wave forms, deflecting ions with $L > L_*$ into the wake region through a Prandtl-Meyer expansion fan structure; the underlying process driven by electrostatic pressure. The resulting wave structure is defined by the ion acoustic wave angle θ_r, such that [50],

$$\begin{aligned} \theta_r &= \sin^{-1}\left(\frac{1}{M_i}\right) \\ M_i &= \frac{v_\infty}{\sqrt{k_B(T_e + \gamma T_i)/m_i}} \end{aligned} \tag{27}$$

where γ is the adiabatic index described as $\gamma =$

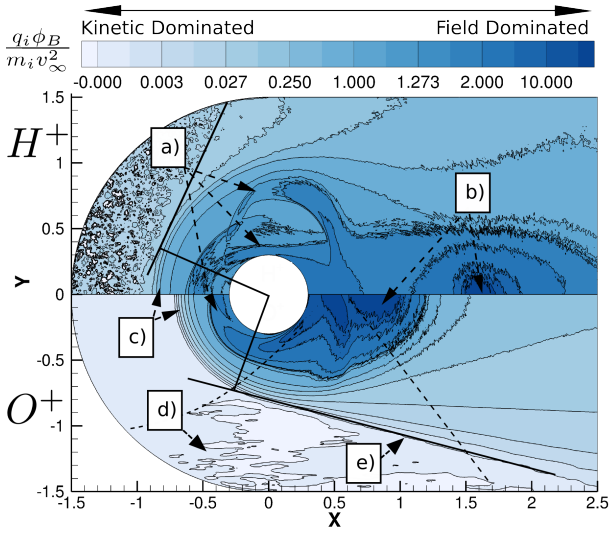

Figure 17: Contours of potential to kinetic energy ratio for H^+ (top) and O^+ (bottom) flow. Features are labels are as follows: a) bounded ion jets, b) detached ion void region, c) compressed fore-body region, d) unbounded ion jets, e) rarefaction wave angle.

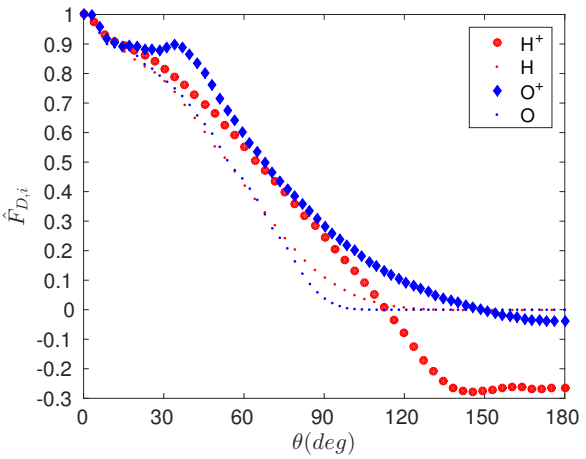

Figure 18: Normalised ion drag force distribution for $\phi_B = -50$ V cylinder in H^+ and O^+ plasma.

$1 + 2/n$ where n is the degrees of freedom; $\gamma = 2$ for this work.

Taking into account ion thermal velocity, the ion acoustic Mach number in the O^+ flow is $M_i = 4.61 \pm 0.77$. From Eqn. 27, θ_r should be $12.5^o \pm 2.5^o$ - the ion thermal velocity $v_{t,i}$ acting to diffuse the wave edge. Measured rarefaction wave angle measurements are indicated in Figure 17. θ_r in the O^+ flow is $14.7^o \pm 1^o$, showing reasonable agreement with the predicted wave angle. θ_r measurements in case 8 are more difficult, a reflection of the effect of v_{t,H^+}.

The bulk flow velocity in H^+ predicts an M_i of 1.1583. v_{t,H^+} however is 5 km/s. In other words, the spread of velocity is in the range $2.5\text{km/s} \leq v_B \leq 12.5\text{km/s}$. Therefore, while the majority of the flow is supersonic ($M_i > 1$), there exists a subset of the ion population which is subsonic ($M_i < 1$). The increased noise in H^+ simulations is a reflection of this subsonic flow element, while the reduced ion mass makes H^+ flows more sensitive to thermal effects. Based on indicated measure in Figure 17, which describes the edge of *"noisey"* freestream region, $theta_r = 63^o \pm 10^o$ - the large uncertainty reflected in the simulation noise. Compared with a predicted $theta_r$ of $59^o \pm 29^o$ this appears to compare well with the bulk flow.

The localized fore-body ion density peak in the O^+ flow is the result of ions deflected through the near-wake with insufficient kinetic energy to escape the sheath dominated region i.e. $L(v) < L_*$ and $r_c < r_B$. Conversely, an unbounded ion jet is formed by the deflection of ions through the near-wake with $r_c > r_B$. A similarly bounded ion jet is evident in H^+ flow; the inherently lower kinetic energy of the H^+ resulting in the capture of the unbounded ions in the O^+ case.

Figure 18 illustrates the effect of these bounded ion jets on the normalised surface drag force distribution $\hat{F}_{D,i}$; gas-surface interaction are treated as in Section 4.2. The equivalent neutral simulations have been included for reference. Both O^+ and H^+ simulations exhibit an increased drag compared to the neutral simulations. In the O^+ case, the ion jet connecting between 28^o and 48^o causes a localized increase in dCPD. Taking the difference between the O^+ and H^+ distribution, the O^+ ion jet causes a 4.4% increase in total O^+ dCPD. Similarly, the H^+ ion thrust is 23.7% of the total H^+ dCPD. In other words, the H^+ thrust negates almost a quarter of the H^+ dCPD.

While OM theory predicts the presence of some of these structures, to date, there exists no treatment of the charged aerodynamics of high voltage LEO objects. Figure 18 presents the first self-consistent treatment of this problem, showing that the effect of kinetic structures such as bounded ion jets have an appreciable influence on surface force distributions.

6. Conclusions and Future Work

In this work, the implementation, validation, and verification of the electrostatic PIC-DSMC code, pdFOAM, has been presented. Developed in OpenFOAM as an extension of the DSMC code dsmcFOAM, the purpose of pdFOAM is to study the physical interaction of near-Earth objects and the space environment, including both neutral and charged species. A series of validation cases were presented demonstrating the ability of pdFOAM to reproduce rarefied gas dynamic and plasma phenomena. The final part of this paper considered the influence of dCPD on a 2D cylinder with fixed floating potential of $-50V$ in O^+ and H^+ plasmas representative of Ionospheric conditions. A discrete ion jet in the O^+ case was observed to cause a 4.4% increase in dCPD. A class of bounded ions not considered by OM theory in the H^+ case was observed to a cause direct thrust force equivalent to 23.7% of the total H^+ dCPD. These results provide new insights into the role of bounded ion jets to dCPD in LEO. Ultimately, pdFOAM represents a novel research tool that can be used to explore the interaction of LEO objects with the near-Earth space environment.

Acknowledgements

This research was undertaken with the assistance of resources from the National Computational Infrastructure (NCI), which is supported by the Australian Government.

References

[1] Allen, J. E., 1992. Probe theory - the orbital motion approach. Physica Scripta 45 (5), 497–503.

[2] Al'Pert, Y. L., Gurevich, A. V., Pitaevskii, L. P., 1965. Space Physics with Artificial Satellites. Consultants Bureau, New York.

[3] Anderson, P. C., 2012. Characteristics of spacecraft charging in low Earth orbit. Journal of Geophysical Research 117 (A7), 1–11.

[4] Andres, I. J., 2007. Enhanced Modelling of LAGEOS Non-Gravitational Perturbations. Sieca Repro, Turbineweg, Delft.

[5] Auweter-Kurtz, M., Fertig, M., Petkow, D., Stindl, T., Quadt, M., Munz, C.-D., Adamidis, P., Resch, M., Roller, S., D'Andrea, D., Schneider, R., 2005. Development of a hybrid PIC/DSMC Code. In: 29 th International Electric Propulsion Conference,. pp. 1–15.

[6] Bird, G. A., 1976. Molecular Gas Dynamics. Clarendon Press, Oxford.

[7] Bird, G. A., 1994. Molecular Gas Dynamics and Direction Simulation of Gas Flows. Clarendon Press.

[8] Bird, G. A., 2007. Sophisticated DSMC. In: DSMC07 meeting. pp. 1–49.

[9] Bird, G. A., 2013. The DSMC Method, 1st Edition. CreateSpace, Sydney.

[10] Birdsall, C. K., Langdon, A. B., 1991. Plasma physics via computer simulation. Vol. 42. Adam Hilger Press, New York.

[11] Boerner, J., Boyd, I. D., 2007. Numerical Simulation of Probe Measurements in a Non-equilibrium Plasma , Using a Detailed Model Electron Fluid. AIAA Aerospace Science Meeting and Exhibit 2007-995 (January), 1–12.

[12] Boltzmann, L., 1872. Weitere StudiEn fiber das WSxmegleichgewicht unter Gasmolekfilen. Wien. Ber.

[13] Brieda, L., Kafafy, R., Pierru, J., Wang, J., 2004. Development of the DRACO Code for Modeling Electric Propulsion Plume Interactions (July).

[14] Brundin, C. L., 1963. Effects of Charged Particles on the Motion of an Earth Satellite. AIAA Journal 1 (11), 2529–2538.

[15] Chopra, K. P., 1961. Errata: Interactions of Rapidly Moving Bodies in Terrestrial Atmosphere. Review of Modern Physics 33 (2).

[16] Chopra, K. P., 1961. Interactions of Rapidly Moving Bodies in Terrestrial Atmosphere. Review of Modern Physics 33 (2).

[17] Daugherty, J. E., Porteous, R. K., Kilgore, M. D., Graves, D. B., 1992. Sheath structure around particles in low-pressure discharges. Journal of Applied Physics 72 (9), 3934–3942.

[18] Delzanno, G. L., Camporeale, E., David Moulton, J., Borovsky, J. E., MacDonald, E. a., Thomsen, M. F., 2013. CPIC: A curvilinear particle-in-cell code for plasma-material interaction studies. IEEE Transactions on Plasma Science 41 (12), 3577–3587.

[19] Dietrich, S., Boyd, I. D., 1996. Scalar and Parallel Optimized Implementation of the Direct Simulation Monte Carlo Method. Journal of Computational Physics 126 (2), 328–342.
URL `http://www.sciencedirect.com/science/article/pii/S0021999196901412`

[20] Fehske, H., Schneider, R., Weibe, A., 2008. Computaional Many-particle Physics. Springer, New York.

[21] Feller, W., 1940. On the Integro-Differential Equations of Purely Discontinuous Markoff Processes 48 (3), 488–515.

[22] Forest, J., Hilgers, A., Thiébault, B., Eliasson, L., Berthelier, J. J., De Feraudy, H., 2006. An open-source spacecraft plasma interaction simulation code PicUp3D: Tests and validations. IEEE Transactions on Plasma Science 34 (5 II), 2103–2113.

[23] Fortov, V. E., Ivlev, A. V., Khrapak, S. A., Khrapak, A. G., Morfill, G. E., 2005. Complex (dusty) plasmas: Current status, open issues, perspectives. Physics Reports 421 (1-2), 1–103.

[24] Fournier, G., 1970. Electric drag. Planetary and Space Science 18 (7), 1035–1041.

[25] Garrett, H. B., 1981. The charging of spacecraft surfaces. Review of Geophysics and Space Physics, 19 (4), 577–616.

[26] Garrett, H. B., Whittlesey, A. C., 2000. Spacecraft charging, an update. IEEE Transactions on Plasma Science 28 (6), 2017–2028.

[27] Godd, R., Laframboise, J. G., 1983. Total current to cylindrical collectors in collisionless plasma flow. Planetary and Space Science 31 (3), 275–283.

[28] Hastings, D. E., 1995. A review of plasma interactions with spacecraft in low Earth orbit. Journal of Geophysical Research 100 (A8), 14457–14483.

[29] Hastings, D. E., Garrett, H. B., 1996. Spacecraft-Environment Interactions. Cambridge University Press.

[30] Hockney, R. W., Eastwood, J. W., 1988. Computer Simulation Using Particles. Taylor & Francis Group, Abingdon.
URL http://link.aip.org/link/SIREAD/v25/i3/p425/s1{&}Agg=doi

[31] Hoegy, W. R., Wharton, L. E., 1973. Current to a moving cylindrical electrostatic probe. Journal of Applied Physics 44 (12), 5365–5371.

[32] Hutchinson, I. H., 2004. Ion collection by a sphere in a flowing plasma: 3. Floating potential and drag force. Plasma Physics and Controlled Fusion 47 (1), 71–87.

[33] Jasak, H., Jemcov, A., Tukovic, Z., 2007. OpenFOAM : A C ++ Library for Complex Physics Simulations. International Workshop on Coupled Methods in Numerical Dynamics m, 1–20.

[34] Jastrow, R., Pearse, C. A., 1957. Atmospheric Drag on the Satellite. Journal of Geophysical Research 62 (3).
URL http://onlinelibrary.wiley.com/doi/10.1029/JZ062i003p00413/pdf

[35] Kolobov, V. I., Arslanbekov, R. R., 2012. Towards adaptive kinetic-fluid simulations of weakly ionized plasmas. Journal of Computational Physics 231 (3), 839–869.
URL http://dx.doi.org/10.1016/j.jcp.2011.05.036

[36] Koons, H. C., Mazur, J. E., Selesnick, R. S., Blake, J. B., Fennell, J. F., Roeder, J. L., Anderson, P. C., 2000. The impact of the space environment on space systems. 6th Spacecraft Charging Technology Conference (September), 7–11.
URL http://oai.dtic.mil/oai/oai?verb=getRecord{&}metadataPrefix=html{&}identifier=ADA376872

[37] Lapenta, G., 2011. DEMOCRITUS: An adaptive particle in cell (PIC) code for object-plasma interactions. Journal of Computational Physics 230 (12), 4679–4695.
URL http://dx.doi.org/10.1016/j.jcp.2011.02.041

[38] Lofthouse, A. J., Holman, T. D., Boyd, I. D., 2011. Effects of continuum breakdown on hypersonic aerothermodynamics for reacting flow. Physics of Fluids 23 (2).

[39] Macpherson, G. B., Niklas, N., Weller, H. G., 2009. Particle tracking in unstructured, arbitrary polyhedral meshes for use. International Journal for Numerical Methods in Biomedical Engineering 25, 263–273.
URL http://onlinelibrary.wiley.com/doi/10.1002/cnm.1494/full

[40] Maxwell, J. C., Trans, P., Lond, R. S., 1867. On the Dynamical Theory of Gases (January), 49–88.

[41] McMahon, J. C., Xu, G. Z., Laframboise, J. G., 2005. The effect of ion drift on the sheath, presheath, and ion-current collection for cylinders in a collisionless plasma. Physics of Plasmas 12 (6), 1–11.

[42] Miloch, W. J., Yaroshenko, V. V., Vladimirov, S. V., Pecseli, H. L., Trulsen, J., 2012. Spacecraft charging in flowing plasmas. In: Journal of Physics: Conference Series.

[43] Olson, S. E., Christlieb, A. J., 2008. Gridless DSMC. Journal of Computational Physics 227, 8035–8064.

[44] Pfeiffer, M., Mirza, A., Fasoulas, S., 2013. A grid-independent particle pairing strategy for DSMC. Journal of Computational Physics 246, 28–36.
URL http://dx.doi.org/10.1016/j.jcp.2013.03.018

[45] Riemann, K. U., 1991. The Bohm criterion and sheath formation. Journal of Physics D: Applied Physics 24 (4), 493–518.
URL http://stacks.iop.org/0022-3727/24/i=4/a=001?key=crossref.8ef018f33cb54573928abc7217c3932b

[46] Sadarjoen, I. A., van Walsum, T., Hin, A. J. S., Post, F. H., Sadarjoen, A., Walsum, T. V., Post, F. H., 1994. Particle Tracing Algorithms for 3D Curvilinear Grids. Tech. rep., Delft.

[47] Scanlon, T. J., Palharini, R. C., White, C., Ezpinoza, D., Casseau, V., 2015. Simulation of Rarefied and Continuum Hypersonic Flow over Re-Entry Objects. European Symposium on Aerothermodynamics for Space Vehicles.

[48] Scanlon, T. J., Roohi, E., White, C., Darbandi, M., Reese, J. M., 2010. An open source, parallel DSMC code for rarefied gas flows in arbitrary geometries. Computers and Fluids 39 (10), 2078–2089.
URL http://dx.doi.org/10.1016/j.compfluid.2010.07.014

[49] Schwager, L. a., Birdsall, C. K., 1990. Collector and source sheaths of a finite ion temperature plasma. Physics of Fluids B: Plasma Physics 2 (5), 1057–1068.
URL http://link.aip.org/link/?PFB/2/1057/1

[50] Stone, N. H. N., 1981. The Aerodynamics of Bodies in a Rearefied Ionized Gas with Applications to Spacecraft Environmental Dynamics. Tech. rep., Marshall Space Flight Center, Alabama.

[51] Uglov, A., Gnedovets, A., 1991. Effect of particle charging on momentum and heat transfer from rarefied plasma flow. Plasma chemistry and plasma processing 11 (2), 251–267.
URL http://www.springerlink.com/index/W818014518V61PH2.pdf

[52] Wagner, W., 1992. A convergence proof for Bird's direct simulation Monte Carlo method for the Boltzmann equation. Journal of Statistical Physics 66 (3-4), 1011–1044.

[53] Wang, J., 1991. Electrodynamic Interactions Between Charged Space Systems and the Ionospheric Plasma Environment. Ph.D. thesis, Massachusetts Institute of Technology.

[54] Wang, J., Hastings, D. E., 1992. Ionospheric plasma flow over large high-voltage space platforms. II: The formation and structure of plasma wake. Phys. Fluids B 4 (6), 1597–1614.

[55] Wang, J., Qiu, J. W., Qin, X. G., 2008. PIC Simulation of Surface Charging in the Wake Zone. In: PIERS Proceedings. Hangzhou, China, pp. 518–521.

[56] Whipple, E. C., 1965. The Equilibrium Electric Potential of a Body in the Upper Atmosphere and in Interplanetary Space. Ph.D. thesis, George Washington University.

[57] Whipple, E. C., 1981. Potentials of surfaces in space. Reports on Progress in Physics 44 (11), 1197–1250.
URL http://iopscience.iop.org/0034-4885/44/11/002